Physics of Fluids

Shear-dependent microvortices in liquid–liquid flow-focusing geometry: A theoretical, numerical, and experimental study

Cite as: Phys. Fluids **33**, 032016 (2021); https://doi.org/10.1063/5.0039179
Submitted: 30 November 2020 . Accepted: 13 February 2021 . Published Online: 23 March 2021

Gopakumar Kamalakshakurup, Mohammad Aghaamoo, Marzieh Ataei, Naiqing Zhang (张乃卿), and Abraham P. Lee

Physics of Fluids ARTICLE scitation.org/journal/phf

Shear-dependent microvortices in liquid–liquid flow-focusing geometry: A theoretical, numerical, and experimental study

Cite as: Phys. Fluids **33**, 032016 (2021); doi: 10.1063/5.0039179
Submitted: 30 November 2020 · Accepted: 13 February 2021 ·
Published Online: 23 March 2021

View Online Export Citation CrossMark

Gopakumar Kamalakshakurup,[1,2] Mohammad Aghaamoo,[1,2] Marzieh Ataei,[2,3] Naiqing Zhang (张乃卿),[4] and Abraham P. Lee[1,2,3,a)]

AFFILIATIONS

[1]Department of Biomedical Engineering, University of California Irvine, Irvine, California 92697, USA
[2]Center for Advanced Design and Manufacturing of Integrated Microfluidics (CADMIM), University of California Irvine, Irvine, California 92697, USA
[3]Department of Mechanical and Aerospace Engineering, University of California Irvine, Irvine, California 92697, USA
[4]Department of Mechanical and Aerospace Engineering, University of California San Diego, San Diego, California 92161, USA

[a)]Author to whom correspondence should be addressed: aplee@uci.edu

ABSTRACT

In this work, we describe the mechanism of particle trapping and release at the flow-focusing microfluidic droplet generation junction, utilizing the hydrodynamic microvortices generated in the dispersed phase. This technique is based solely on our unique flow-focusing geometry and the flow control of the two immiscible phases and, thus, does not require any on-chip active components. The effectiveness of this technique to be used for particle trapping and the subsequent size selective release into the droplets depends on the fundamental understanding of the nature of the vortex streamlines. Here, we utilized theoretical, computational, and experimental fluid dynamics to study in detail these microvortices and parameters affecting their formation, trajectory, and magnitude.

I. INTRODUCTION

Droplet microfluidic technology has evolved into a powerful platform for performing single cell analysis,[1] nucleic acid sequencing,[2,3] cytotoxicity screening,[4] and directed evolution of biomolecules.[5] Most of these applications require controlled confinement of cells, particles, and biomolecules in pl–nl droplets. Therefore, cell/particle manipulation techniques are essential to achieve these operations. Generally, particle manipulation techniques can be classified into active or passive control designs. Active techniques include dielectrophoretic,[6,7] magnetophoretic,[8] acoustophoretic,[9,10] thermophoretic,[11] and optical methods.[12,13] These techniques require active components such as electrodes and actuators to perform the operation.[14,15] In contrast, passive techniques do not require additional on-chip transducers and rely on hydrodynamic flow control, which include inertial,[16–18] viscoelastic,[19] pinched flow fractionation,[20] and gravitational fields.[21,22]

Passive single cell/particle encapsulation in droplets is realized by both deterministic and nondeterministic methods.[23] In nondeterministic methods, single cell encapsulation in droplets is often dictated by Poisson statistics. The nonuniform spatial distribution and random arrival time of cells at the droplet generation junction often add uncertainty to whether a droplet contains a single cell, multiple cells, or no cells at all.[24] Within the Poisson regime, the cell concentration and the relative flow rates of the dispersed and continuous phase are typically optimized to achieve improved single cell encapsulation efficiency. On the other hand, the deterministic methods leverage unique hydrodynamic flow control techniques to overcome the Poisson hurdle.[25] One such technique employs the Rayleigh–Plateau instability jet breakup where the cell-encapsulated droplets have a larger diameter than the empty droplets. Using lateral induced drift and steric interactions between the droplets at the bifurcation, larger droplets with single cells are sorted at 79.2% efficiency.[26] Another technique utilizes the Rayleigh–Plateau instability jet breakup along with DLD (Deterministic Lateral Displacement) pillar arrays to sort large-sized single-cell encapsulated droplets from the small empty ones.[27] High efficiency single cell encapsulation can also be achieved using inertial ordering. Incorporating a long, high aspect ratio microchannel[28] or a spiral channel[29] upstream improves the single cell encapsulation efficiency up to 80%. However, the requirement of high cell

concentrations and the need to synchronize the ordered cells with the droplet generation rate add complexity to the technique. To perform single cell encapsulation at low cell concentrations and when the sample contains various-sized cells or particles, the techniques listed above often fall short. In 2017, our lab reported a microvortex based technique that can trap and release cells/particles into droplets based on their sizes.[30] In this method, an "expansion" flow-focusing design is used for droplet generation.[31] By applying high shear stress on the interface of the continuous/dispersed phases near the narrow orifice, we could demonstrate the formation of two symmetric three-dimensional microvortices in the dispersed phase. These microvortices were, then, used for trapping cells, enriched their concentration locally, and then released them one-to-one (1–1) into droplets at >50% encapsulation efficiency, which is at least 10 times greater efficiency than random encapsulations at low sample concentrations.

To improve the effectiveness and robustness of this method, here we utilize experimental, theoretical, and computational fluid dynamics (CFD) to focus our discussion on understanding the physics of such microvortices and their key control parameters. Using experimental fluid mechanics, we study the mechanism for generating microvortices and quantitatively evaluate the microvortex trapping size threshold (d_{gap}) for selective trap and release of particles. In addition, we present a theoretical model to predict parameters affecting the microvortex trapping size threshold (d_{gap}) and validate it with experimental results. Since the inherent three-dimensional nature of these complex vortices makes it challenging to only rely on experimental and theoretical fluid mechanics for such studies, a 3D computational fluid dynamics (CFD) model using the volume of fraction (VOF) multiphase algorithm is, then, developed to capture the three-dimensional nature of such vortex streamlines. Utilizing the developed CFD model, we study the effect of various parameters [e.g., channel geometry, capillary number (Ca), and contact angle] on the microvortices. The present theoretical and CFD study supported by experimental results provide detailed understanding of shear-dependent microvortices in liquid–liquid flow-focusing designs, which can be used for developing more efficient 1–1 droplet encapsulation methods.

II. THEORETICAL MODEL

Figure 1(a) shows the schematic of the device illustrating the fluidic circuits for both continuous (oil) and dispersed (aqueous) phases and the microvortex streamlines generated in the dispersed phase. The continuous phase enters the junction through the side channels and exits through the narrow orifice, shearing the dispersed phase. The occurrence of the microvortices (in the aqueous phase) depends on the combined effect of the aqueous–oil interfacial shearing rate (α) and the tip oscillation frequency (TOF), defined as the interfacial oscillation frequency of the droplet generation tip. The protrusion and retraction (from the P1 to the P2 position) of the droplet generation tip occur each time a droplet is generated [Fig. 1(c)]; therefore, the tip oscillation frequency (TOF) is equal to the number of droplets generated per second (f).

Both the parameters α and TOF vary with the droplet generation regime and are affected by viscosity, the flow rate ratio of the dispersed to the continuous phase, interfacial tension, and channel geometry (e.g., orifice width and channel height). Specifically, α and TOF are the smallest in the squeezing regime and the highest in the jetting regime, which is dictated by the capillary number ($Ca = \frac{\mu_c V_c}{\gamma}$), where μ_c is the viscosity of the continuous phase, V_c is the velocity of the continuous phase, and γ is the interfacial tension between the phases.[32] In our previous work, we observed that microvortices start to occur at higher values of α and TOF.[30] In the squeezing regime, which occurs at lower Ca, both the interfacial shearing rate (α) and the TOF (<100 Hz) are not large enough to generate the microvortices. However, at a higher Ca value (where the regime switches from squeezing to dripping), the microvortices are likely to occur because of the increase in α and TOF (>2000 Hz). Dynamics of the vortex streamlines in dripping and jetting is nearly the same; therefore, we focus our discussion on the squeezing and dripping regimes.

In the dripping regime, the microvortices can be formed by tuning α and TOF. Once they are formed, the dispersed phase enters the control volume through the center channel inlet, recirculates within the vortex, and exits through d_{gap} out of the orifice as droplets [Fig. 1(a)], where d_{gap} is the width that separates the closed vortex streamline from the interface [Fig. 1(b)].[33,34] The rapid pulsing of aqueous interface during the droplet formation is analogous to the air–aqueous interface vibration in the microstreaming flows. The recirculation vortices are directed such that they are forward-oriented at the interface and reverse-oriented at the center.

The expression for d_{gap} can be derived with the assumption that d_{gap} is approximately equal to the radius of the dispersed phase thread (R_{thread}) in the dripping regime [Fig. 1(b)],

$$d_{gap} \cong R_{thread}. \tag{1}$$

This is a fair physics assumption since the microvortices end near the thread. Based on the theoretical work developed by Tomotika and Taylor,[35] R_{thread} can be related to the size of generated droplets ($R_{droplet}$) as

$$R_{thread} = \frac{1}{\left(\frac{1.5\pi}{X_m}\right)^{\frac{1}{3}}} R_{droplet}, \tag{2}$$

where dimensionless parameter X_m is the dominant wave number. X_m can be expressed in terms of dominant wavelength λ_m, at which the maximum instability occurs at the thread,

$$X_m = \frac{2\pi R_{thread}}{\lambda_m}. \tag{3}$$

Based on Eq. (2) and from the tabulated values for X_m by Tomotika *et al.*, for the viscosity ratio ($\frac{\mu_d}{\mu_c}$) of 0.025, used in this study, we have

$$R_{thread} = 0.3\, R_{droplet}. \tag{4}$$

In flow-focusing geometries, there exists a power-law relation between the dimensionless droplet size ($\frac{R_{droplet}}{W_{orifice}}$, where $W_{orifice}$ is the orifice width) and the flow rates of continuous and dispersed phases (Q_c and Q_d, respectively),

$$\frac{R_{droplet}}{W_{orifice}} \propto \left(\frac{Q_d}{Q_c}\right)^{\beta}, \tag{5}$$

where β usually lies in the range of 0.25–0.35.[31,36] For our specific microchannel geometry, β is equal to 0.3.[31] Using Eqs. (1) and (4), this power-law relation can be rewritten as

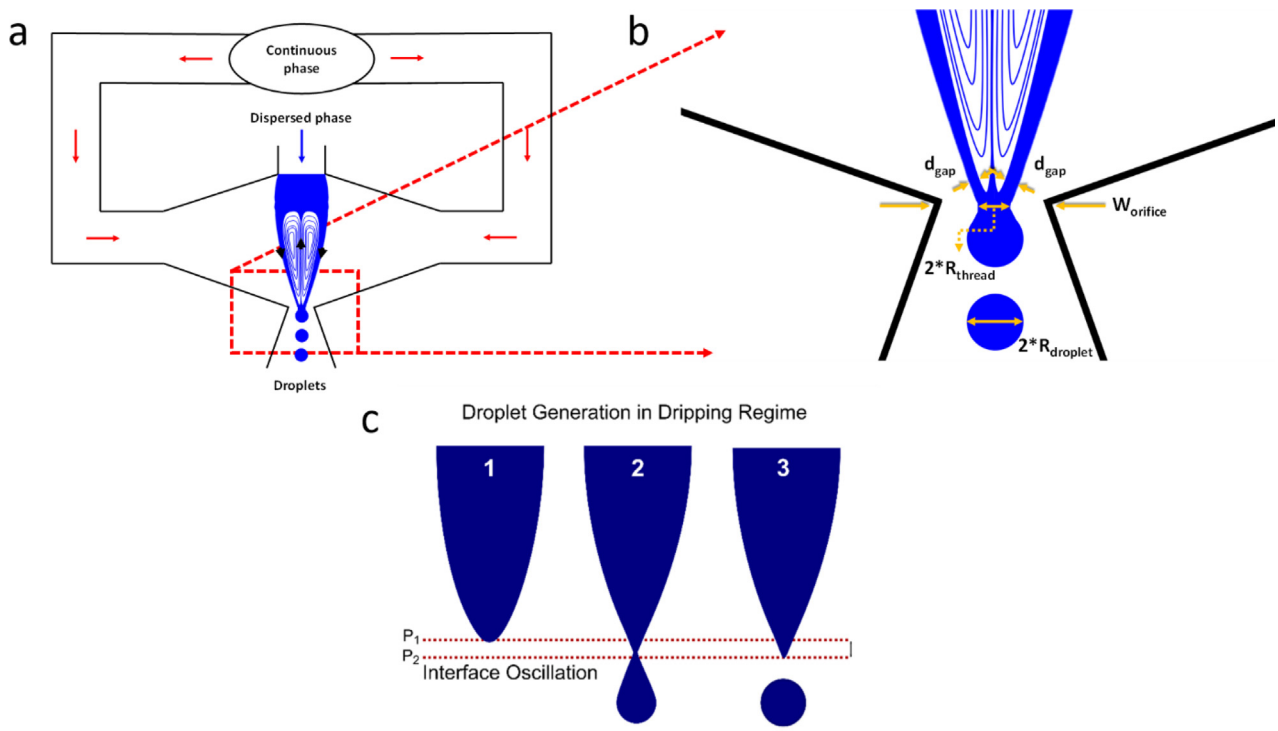

FIG. 1. (a) Schematic of the fluidic circuit and the flow-focusing junction along with the microvortices generated in the dispersed phase; d_{gap} is shaded in blue. (b) Zoomed in schematic of the droplet generation junction illustrating the relevant parameters. (c) Schematic illustration of the tip oscillation during the droplet formation. The dispersed phase tip oscillates between P1 and P2 each time when a droplet is generated—an important parameter for the generation of the microvortices.

$$d_{gap} = 0.3C_1.W_{orifice}.\left(\frac{Q_d}{Q_c}\right)^{0.3}, \tag{6}$$

where the constant C_1 is dependent on microchannel geometry and can be derived empirically or numerically. Based on Eq. (6), if the flow rate of the dispersed phase is fixed, d_{gap} has an inverse power-law correlation with the capillary number $[d_{gap} \propto \left(\frac{1}{Ca}\right)^{0.3}]$ because the capillary number is directly related to the continuous phase flow velocity.

III. NUMERICAL MODEL

Transient modeling of droplet generation is performed using the commercial CFD package ANSYS Fluent. The device 3D geometry was built using the ANSYS Design Modeler and meshed in ANSYS Meshing. The 3D mesh mainly consisted of hexahedron elements with quadrilateral 2D elements on surfaces. To accurately capture the droplet generation, the mesh is further refined near wall interfaces using the inflation meshing technique. The device geometry, meshing, and boundary conditions are shown in Fig. 2.

The explicit coupled level-set and volume of fluid (VOF) model was employed to track the interface between the dispersed and continuous phases.[37,38] Such a coupled method overcomes the deficiencies of the level-set model in preserving volume conservation and VOF in the calculation of spatial derivatives. The transient tracking of the level-set function (ϕ) is similar to the VOF model and can be written as

$$\frac{\partial \phi}{\partial t} + \nabla.(\vec{u}\phi) = 0, \tag{7}$$

where $\vec{u}$ is the velocity field, and the level set-function can be defined as the signed distance to the interface as follows:

$$\phi(x,t) = \begin{cases} +|d| & if\ x \in the\ primary\ phase \\ 0 & if\ x \in \Gamma = \{x \,|\, \phi(x,t) = 0\} \\ -|d| & if\ x \in the\ secondary\ phase, \end{cases} \tag{8}$$

where d is the distance from the interface. In this work, the primary and secondary phases are the continuous and dispersed phases, respectively. In modeling droplet generation phenomena, there exists significant deformation of interfaces and uneven thickness across them. Thus, large numerical errors can be produced in mass and momentum equations, as distant constraint ($|\nabla\phi| = 1$) cannot be maintained. To circumvent this, a level-set reinitialization process is adopted at each time step based on the geometrical interface-front construction method.[39] In reconstruction of the interface, the VOF model provides information on locating interface fronting cells, and level-set gradients determine the direction of the interface.

In addition, the momentum equation is also solved throughout the domains as follows:

$$\frac{\partial(\rho\vec{u})}{\partial t} + \nabla.(\rho\vec{u}\vec{u}) = -\nabla p + \nabla.\mu\left[\nabla\vec{u} + (\nabla\vec{u})^T\right] - \vec{F}_{sf} + \rho\vec{g}. \tag{9}$$

The term $\vec{F}_{sf}$ in Eq. (9) is the force due to surface tension. Based on the continuum surface force (CSF) model, this term can be written as

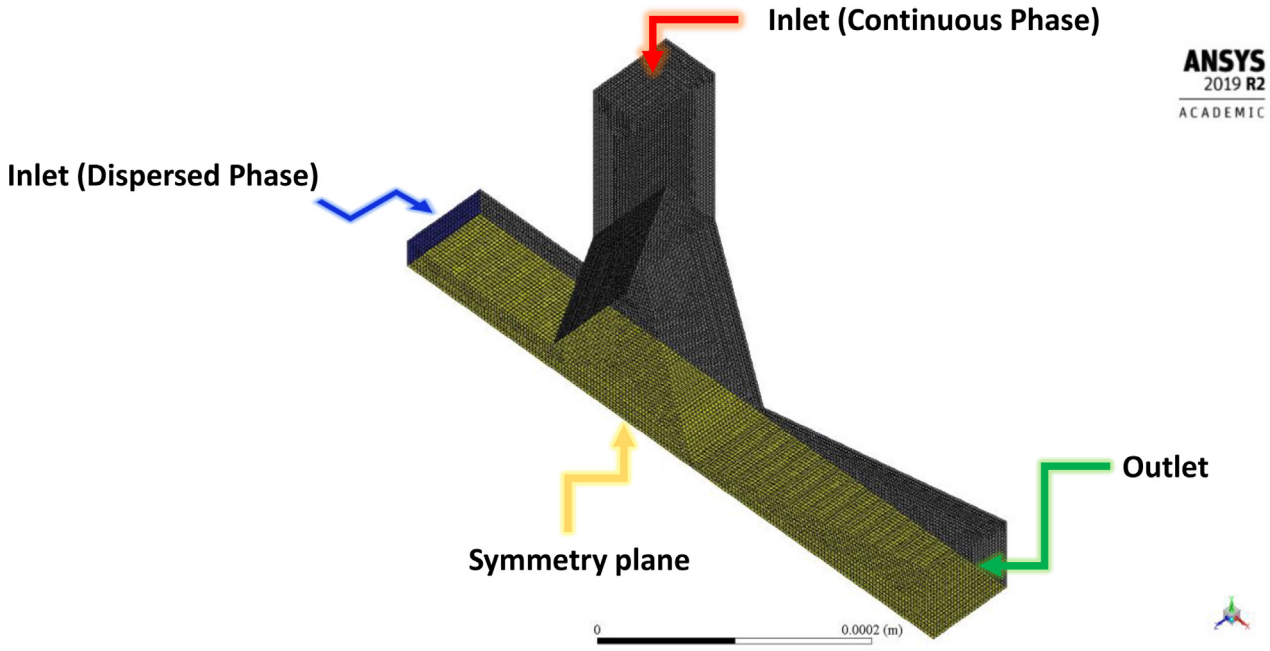

FIG. 2. 3D device geometry with the corresponding meshing performed in ANSYS Meshing and the boundary conditions. For reducing the cost of the calculations, the symmetry boundary condition is chosen. All other boundaries not specified here are walls.

$$\vec{F}_{sf} = \sigma\kappa\delta(\phi)\vec{n}, \tag{10}$$

where σ is the surface tension coefficient, $\kappa = \nabla.\frac{\nabla\phi}{|\nabla\phi|}|_{\phi=0}$ is the local mean interface curvature, $\vec{n} = \frac{\nabla\phi}{|\nabla\phi|}|_{\phi=0}$ is the local interface normal, and

$$\delta(\phi) = \begin{cases} 0 & |\phi| \geq a \\ \dfrac{1+\cos\left(\dfrac{\pi\phi}{a}\right)}{2a} & |\phi| < a, \end{cases} \tag{11}$$

where a is the thickness of the interface. We also adopted the wall adhesion model to include the effect of the contact angle. In this model, the surface normal of the cell next to the wall can be calculated as follows:

$$\vec{n} = \vec{n}_w\cos\theta + \vec{t}_w\sin\theta, \tag{12}$$

where $\vec{n}_w$ and $\vec{t}_w$ are unit vectors normal and tangential to the wall and θ is the contact angle.

The SIMPLEC pressure-based solver was used for solving the flow problem. For the convection term of equations, the Least Squares Cell Based method was adopted for evaluation of gradients. Furthermore, PRESTO! was used for pressure discretization.

In addition, since the Courant number ($C = \frac{\Delta t\, V_{fluid}}{\Delta x}$, where Δt is the time step, Δx is the cell size, and V_{fluid} is the fluid velocity) is an important dimensionless parameter, which greatly influences the stability of numerical simulation in multiphase flow problems, the adaptive time stepping algorithm was used to hold the maximum C number to 0.25 throughout the simulation.

IV. EXPERIMENTAL METHODS

A. Device fabrication

The microfluidic device is fabricated in polydimethylsiloxane (PDMS) by soft lithography. The device was sealed by placing PDMS in contact with glass cover slides after oxygen plasma treatment. The assembled device was left in an oven at 120 °C long enough to restore PDMS hydrophobicity. The contact angle of aqueous solution used in our study on PDMS was measured to be 140°.[40] An illustration of the setup is shown in Fig. 3. For the device used in the experiments, the channel height is 75 μm, as measured using a profilometer.

B. Solution preparation

Ethyl oleate and 2% ABIL EM 90 form the continuous phase ($\rho_c = 838\,\frac{\text{kg}}{\text{m}^3}$ and $\mu_c = 0.04\,\text{Pa}\cdot\text{s}$), and the mixture of water, lipid, glycerol, and surfactant form the dispersed phase ($\rho_d = 1000\,\frac{\text{kg}}{\text{m}^3}$, $\mu_d = 0.001\,\text{Pa}\cdot\text{s}$). Briefly, 5 mg DSPC (1,2-distearoyl-sn-glycero-3-phosphocholine, Avanti Polar Lipids) and 1.96 mg DSPE-PEG2000 {1,2-distearoyl-sn-glycero-3-phosphoethanolamine-*N*-[methoxy-(polyethylene glycol)-2000], Avanti Polar Lipids} were combined in a glass vial and dissolved in chloroform (CHCl3, Sigma) to form a homogeneous mixture. The solvent was evaporated with a nitrogen stream. 4 ml of ultrapure water was added to the dry lipid mixture and sonicated at 50 °C for 20 min. The solution was combined with an additional 4 ml of glycerol (Sigma) and 2 ml of nonionic surfactant (Pluronic F-68, Sigma), sonicated at 50 °C for 20 min. The lipid solution was sonicated again for 15 min immediately prior to use to minimize unwanted liposome formation. The surface tension between the two phases was measured to be 35 $\frac{\text{mN}}{\text{m}}$.

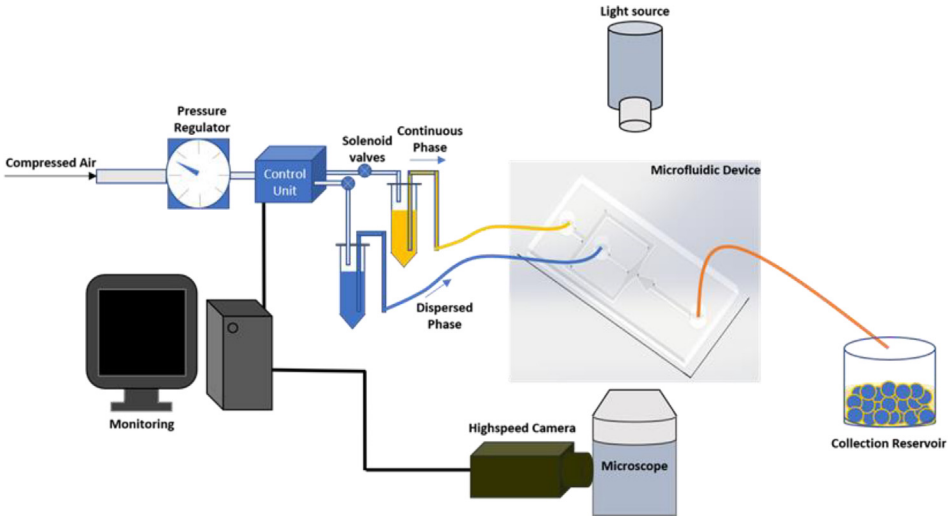

FIG. 3. Experimental setup demonstration for the static-pressure pumping approach. The microfluidic device is placed on an inverted microscope attached to a high-speed camera for visualization purposes. The fluids are driven to the device using our house-made pressure pump. The air pressure above the fluids is regulated via high-speed solenoid valves controlled using a custom-built Lab View program.

C. Fluid handling

The fluids are driven using syringe pumps or the static pressure pumping approach via house made pressure pumps. As for the pressure pumping approach, the fluids are placed in plastic vials and the air pressure above the fluid is regulated by high speed solenoid valves controlled using a custom-built Lab View^{TM} program. The pressure is measured using a pressure gauge (Swagelok) and is reported to be relative to the atmosphere.

D. Data analysis

The high-speed images are captured using a Phantom camera v310 (Vision Research) through an inverted microscope (Nikon 100S). Image *J* software (National Institutes of Health) is used to analyze the videos frame by frame to yield the data.

V. RESULTS AND DISCUSSION

A. Dynamics of shear-dependent microvortices

Several factors determine the droplet generation regime, α, TOF, and likelihood of microvortex formation. These include viscosity, the flow rate ratio of the dispersed to the continuous phase, interfacial tension, and channel geometry (e.g., orifice width and channel height). By fixing the composition of dispersed and continuous phases, we evaluated the effect of the flow rate ratio and orifice width on the formation of microvortices. For this purpose, we picked three different device versions with orifice widths of 10, 15, and 20 μm. In addition, we fixed the flow rate of the dispersed phase at 0.35 $\frac{\mu L}{min}$ so that the changes in the flow rate ratio could be directly correlated with the changes in the capillary number.

Based on the results [Fig. 4(a)], for a given orifice width, the recirculation vortex streamlines are not formed at low capillary numbers. This is due to the combination of the following three conditions observed in the squeezing regime: (i) the oil flow rate is not strong enough to induce the recirculation streamlines in the aqueous phase; therefore, the aqueous–oil interfacial shearing rate (α) is insignificant; (ii) the mode of droplet generation in the squeezing regime; unlike the dripping regime (where the droplet breakup occurs due to Rayleigh–Plateau instability breakup)—in the squeezing regime—droplet breakup occurs due to the pressure built up in the continuous flow lines due to the obstruction of the orifice by the dispersed phase;[42] and (iii) the tip oscillation frequency (TOF) is low (< 100 Hz). By increasing the flow rate of the continuous phase and, consequently, the capillary number, the regime gradually shifts from squeezing to dripping, where both α and the TOF become significant for the recirculation vortex to be observable. While the high aqueous–oil interfacial shearing rate (α) at the orifice creates the microvortices inside the aqueous phase, high TOF (lower protrusion and retraction of the dispersed phase thread) helps maintaining the stability of the system. This contrasts with the squeezing regime where the high protrusion and retraction of the aqueous tip disrupt the stability of microvortices, if any. These findings indicate that there exists a capillary-number threshold, above which the microvortices are formed in the dripping regime. Furthermore, our experimental results also show that this threshold is higher for wider orifice widths.

3D modeling of droplet generation [Fig. 4(b) (multimedia view)] was performed to obtain flow streams in the flow-focusing junction at various capillary numbers. First, a grid independent study was performed with four different mesh refinement levels, corresponding to 100k (level 4), 500k (level 5), 1M (level 6), and 2M (level 7) mesh elements. The simulation time for these levels was 10, 16, 30, and 42 h, respectively, which indicates the high computational cost of modeling such complex physics. For each mesh refinement level, the total pressure was measured at the center of the orifice, and the percentage difference was calculated compared to the previous level. Based on the results [Fig. 4(c)], we picked mesh refinement level 6 for the rest of the study. The droplet generation modeling was, then, validated with experimental results [Fig. 4(a)] for an orifice width of 15 μm and different capillary numbers. According to the results [Figs. 4(d)–4(f)], our developed numerical model accurately predicts the capillary-number threshold at which the microvortices occur, as both experimental and numerical results predict the capillary-number threshold to be in the range of 0.04–0.06.

In the next step, we numerically explored how the pattern of such microvortices changes at different capillary numbers within the

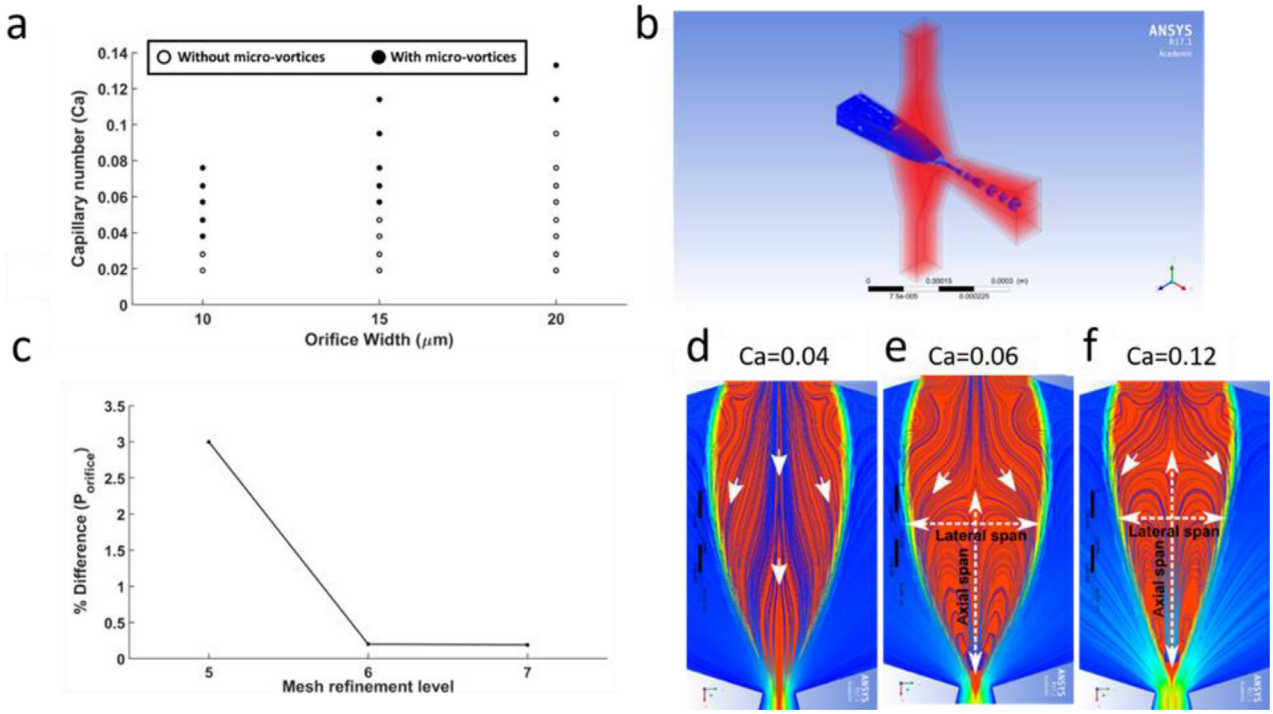

FIG. 4. Dynamics of shear-dependent microvortices. (a) Formation of microvortices as a function of orifice width and capillary number. (b) 3D modeling of droplet generation. (c) Grid independent study of developed numerical modeling. (d)–(f) Numerical modeling results for different capillary numbers. (d) In the squeezing regime, the recirculation vortices are absent; instead, the streamlines are directed toward the orifice as a "through-flow." (e) Increasing *Ca* to 0.06, the droplet generation regime shifts from squeezing to dripping, and the recirculation vortices start to establish. (f) A further increase in the capillary number ($Ca = 0.12$) increases the axial span and decreases the lateral span of the vortices due to the increase in the shearing rate. d_{gap} also decreases moving from (e) to (f). Multimedia views of simulation results for droplet generation in 3D and 2D ($Ca = 0.12$). Multimedia Views: http://dx.doi.org/10.1063/5.0039179.1; http://dx.doi.org/10.1063/5.0039179.2

dripping regime. If *Ca* is relatively small, the rate of continuous shearing is relatively weak, decreasing the axial span of the vortices [Fig. 4(e)]. Also, at this *Ca*, the dispersed phase extends and forms a curved liquid–liquid interface, increasing the lateral span. When the capillary number is further increased, the shear rate imposed by the continuous phase on the dispersed phase is consequently increased, which extends the vortices backward, increasing the axial span [Fig. 4(f) (Multimedia view)]. However, the high rate of shear applied by the continuous phase pushes the dispersed phase symmetrically from all directions, reducing the curvature of the liquid–liquid interface and thereby decreasing the lateral span. Notably, the greater the lateral span, the larger the d_{gap} value. We utilize this capability in performing particle trapping and release operations.

B. Evaluation of microvortex trapping size threshold (d_{gap}) for trap and release of particles

Figure 5 illustrates the generic model describing the particle dynamics in the microvortices. The likelihood of a particle being trapped in microvortices depends on whether its center lines up with vortex streamlines or the streamlines exiting through d_{gap} out of the orifice and into the forming the droplets. The former leads to particle trapping, while the latter results in particle encapsulation in droplets [Fig. 5(a)]. The fundamental principle of such a mechanism is indeed similar to several key hydrodynamic size-based separation techniques such DLD pillar arrays,[43] acoustic streaming,[33,44] and inertial microfluidics.[45]

In our design, once shear-dependent microvortices are formed in the dripping regime, by introducing a particle with radius R_i, particle trapping occurs if $d_{gap} < R_i$, and release occurs when $d_{gap} \geq R_i$, where R_i is the radius of the particle [Fig. 5(a)]. Importantly, we can determine the number of particles releasing into a single droplet. If $d_{gap} \sim R_i$, few droplets contain more than one particle in it. In contrast, as $d_{gap} \gg R_i$, the generated droplets increasingly contain multiple particles.[30] Figure 5(b) (Multimedia view) shows the tracked trajectory of two particles of the same size (10 μm), trapped and recirculating in the two independent vortices [Fig. 5(b) (Multimedia view)]. Except for particle collisions, the continuous recirculation of the particles along its respective streamlines is always observed.

To investigate the trap and release capability, particles with 1 μm size were introduced into the system. Figures 5(c)–5(f) illustrates the simulation and corresponding experimental results for the two operational modes. When the trapping mode is ON ($d_{gap} < 0.5\,\mu m$), the 1 μm particles accumulate in the vortices [Fig. 5(d)]. However, it is observed that the increase in the particle concentration (i) increases the local viscosity of the recirculation fluid according to Einstein's effective viscosity formula,[46] (ii) causes particles to adhere to each other, and (iii) affects the hydrodynamic stability of droplet generation

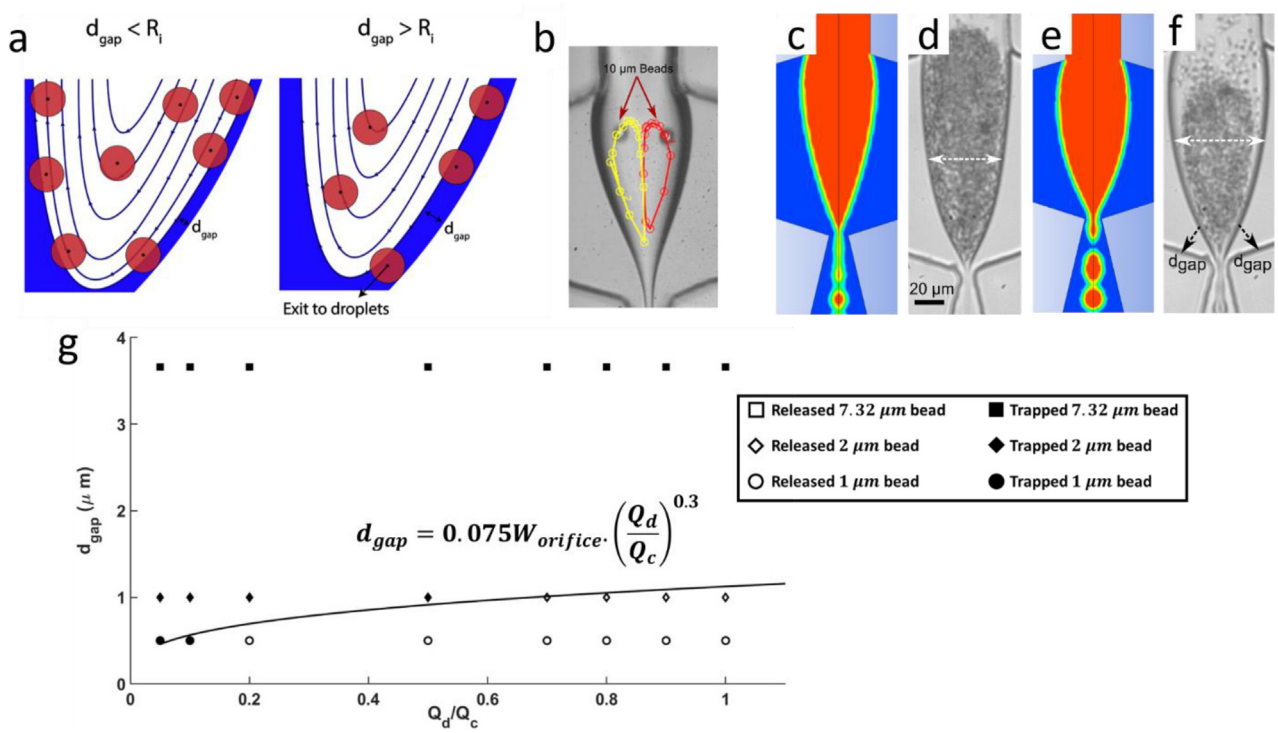

FIG. 5. (a) Schematic illustrating particle dynamics in the vortex streamlines. If $d_{gap} < R_i$, the center of the particles aligns within the vortex streamlines, and thus, trapping occurs. When $d_{gap} \geq R_i$, particles start to be released into the droplets. (b) Particle tracing using Image J. Two 10 μm particles recirculating in two independent vortices over 3 cycles indicate that no trajectory shifting occurs during the recirculation. [(c) and (d)] CFD model and corresponding experimental image of trapping mode, where 1 μm particles are trapped in the vortex. [(e) and (f)] CFD simulation and experimental image of 1 μm particle releasing mode. (g) Theoretical d_{gap} with respect to the flow rate ratios for $W_{orifice} = 15\,\mu m$. The circle, diamond, and square markers (filled: trapped particles and unfilled: released particles) correspond to experimental results for 1 μm, 2 μm, and 7.32 μm polystyrene particles, respectively. Multimedia views: http://dx.doi.org/10.1063/5.0039179.3; http://dx.doi.org/10.1063/5.0039179.4

and results in irregular particle break into the droplets. In this study, we have not investigated the particle–particle interactions and trajectory shift due to collisions. However, by the continuous monitoring of the flow-focusing junction and maintaining particle concentration within the limits, trapping mode ensures 100% trapping of all the particles [Fig. 5(d)]. When $d_{gap} \geq 0.5\,\mu m$, the trapped particles start to be released into the droplets [Fig. 5(f)]. The lateral span in the release mode is greater than that of the trapping mode. This is attributed to the increase in d_{gap} (or the decrease in Ca) due to the increase in the dispersed to continuous pressure ratio. Experimentally, the capillary number Ca (and d_{gap}) is altered by changing the dispersed phase to continuous phase flow rate ratio. It is also observed that d_{gap} does not change instantly to the change in φ, and there exists a transient period before reaching the stability.

In the next step, we evaluated the accuracy of the developed theoretical model in predicting particle trapping and release. According to Eq. (6), there exists a power-law relation between d_{gap} and the flow rate ratio of the dispersed to the continuous phase. Using numerical modeling, the constant C_1 in Eq. (6) was found to be 0.25. For different flow rate ratios of the dispersed to the continuous phase, Fig. 5(g) shows the theoretical values of d_{gap} and experimental data for 1 μm, 2 μm, and 7.32 μm particles. According to Fig. 5(g), there is a relatively good match between experimental and theoretical results. However, Eq. (6) cannot accurately predict the trapping of 1 μm at low flow rate ratios ($\frac{Q_d}{Q_c} < 0.1$). This may be due to the transition of the droplet generation regime to jetting (when $\frac{Q_d}{Q_c} < 0.1$), while the theoretical equation is derived based on the assumption that generation mode is in the dripping regime. In addition, based on the results, for the orifice width of 15 μm, we observed that the release of 7.32 μm beads cannot be achieved while keeping the microvortices stable. Increasing the flow rate ratio to release the 7.32 μm beads increases the likelihood of droplet generetion to switch to the squeezing regime and would result in unwanted instability and, ultimately, disappearance of microvortices.

C. Demonstration of selective trap and release capability

In the dripping regime, by introducing particles of two different sizes (particle A and particle B), three cases are observed: case I: $R_A > d_{gap} < R_B$; case II: $R_A \leq d_{gap} < R_B$; and case III: $R_A \leq d_{gap} \geq R_B$, where R_A and R_B are the radii of particle A and particle B, respectively. In case I, since d_{gap} is smaller than R_A and R_B, both particle A and particle B get trapped in the microvortices [Fig. 6(a)]. However, the dispersed phase continues to exit through the orifice from both the d_{gap} as empty droplets. In case II, since d_{gap} is greater than R_A, particle A exits through d_{gap} into the orifice and encapsulates in the droplets. Here, since d_{gap} is less than R_B, particle B is still unable to go through d_{gap} or encapsulates in the droplets. Consequently,

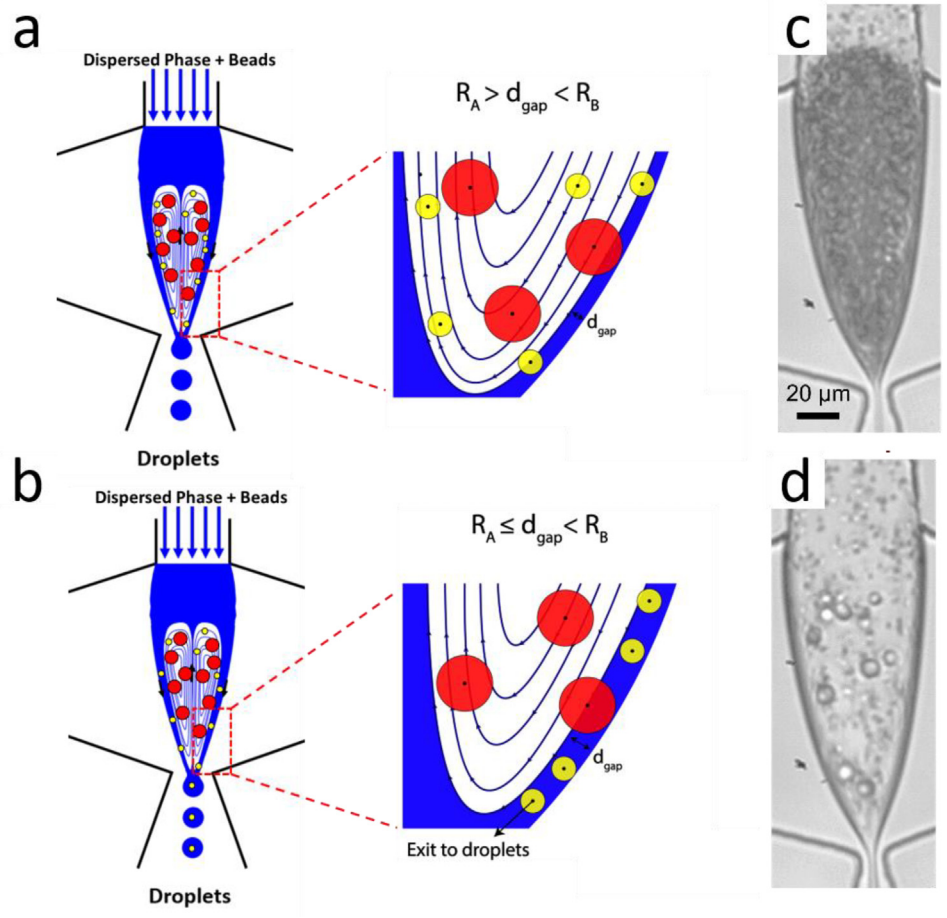

FIG. 6. [(a) and (b)] Schematic illustrating the trap and release capability of the shear-dependent microvortices. When $R_A > d_{gap} < R_B$, microvortices trap both particles. By increasing d_{gap}, so that $R_A \leq d_{gap} < R_B$, smaller particles, "A," are released into droplets, while larger particles, "B," still remain trapped in the microvortices. (c) Trapping of both 1 μm and 7.32 μm particles in the vortices and (d) release of 1 μm particles leaving the 7.32 μm particles trapped in the inner streamlines.

particle B continues to recirculate within the vortex streamline where its center aligns [Fig. 6(b)]. In case III, tuning d_{gap} to be greater than the radius of both particle A and particle B ensures the release of both particles into the droplets. The size selective release of particles is enabled by gradual switching of flow conditions from case I to case III. Notably, the droplet diameter increases with the transition from case I to case III. This is due to the positive correlation between d_{gap} and the droplet diameter, as both increase with the dispersed phase to continuous phase velocity ratio (φ).[31]

To enable the separation of both particle A and particle B, initially d_{gap} is tuned for case I, where both the particles get trapped in the vortices. By switching to case II, particle A is filtered out into the droplets, while particle B still recirculates in the vortices. To release particle B into the droplets, d_{gap} is set to case III. This strategy facilitates the release of particles per the ascending order of their sizes. We have experimentally demonstrated such capability using 1 μm and 7.32 μm diameter polystyrene particles. For this, the dispersed phase containing a mixture of 1 μm and 7.32 μm particles is initially trapped in the vortices [Fig. 6(c)] (case I: 0.5 $\mu m > d_{gap} < 3.66\ \mu m$) and is later released such that distinct release zones can be defined for each particle size by the d_{gap} thresholds. If the setting is for case II ($0.5\ \mu m \leq d_{gap} < 3.66\ \mu m$), the 1 μm particles are released into the droplets, while the 7.32 μm particles remain trapped [Fig. 6(d)].

D. Effect of PDMS surface treatment and channel height on microvortices

Using numerical simulation, we investigated the effect of the PDMS surface treatment and microfluidic channel height on the geometry of microvortices (Fig. 7). The PDMS surface treatment affects the hydrophobicity and, consequently, the contact angle. In this study, we evaluated how microvortices are formed for three different contact angles ($\theta = 120°, 140°$, and $160°$). According to the results [Fig. 7(a)], increasing the hydrophobicity of the microchannels causes the interface between the continuous and dispersed phases to be more convex and, thus, leads to an increase in the lateral span of the microvortices while a decrease in the axial span. In addition, 3D analysis of microvortices indicates that, unlike low-contact angle cases (e.g., $\theta = 120°$) where there exist only two symmetric three-dimensional microvortices [Fig. 7(b) (Multimedia view)], at high contact angles (e.g., $\theta = 160°$), two additional microvortices will be formed at both sides of the main microvortices [Fig. 7(c) (Multimedia view)]. Figure 7(d) shows microvortex geometry for different channel heights. According to the results, by increasing the channel height, the interface becomes more convex in all directions. As a result, both the lateral span and axial span of microvortices increase by increasing the height. These findings indicate that increasing both hydrophobicity and the

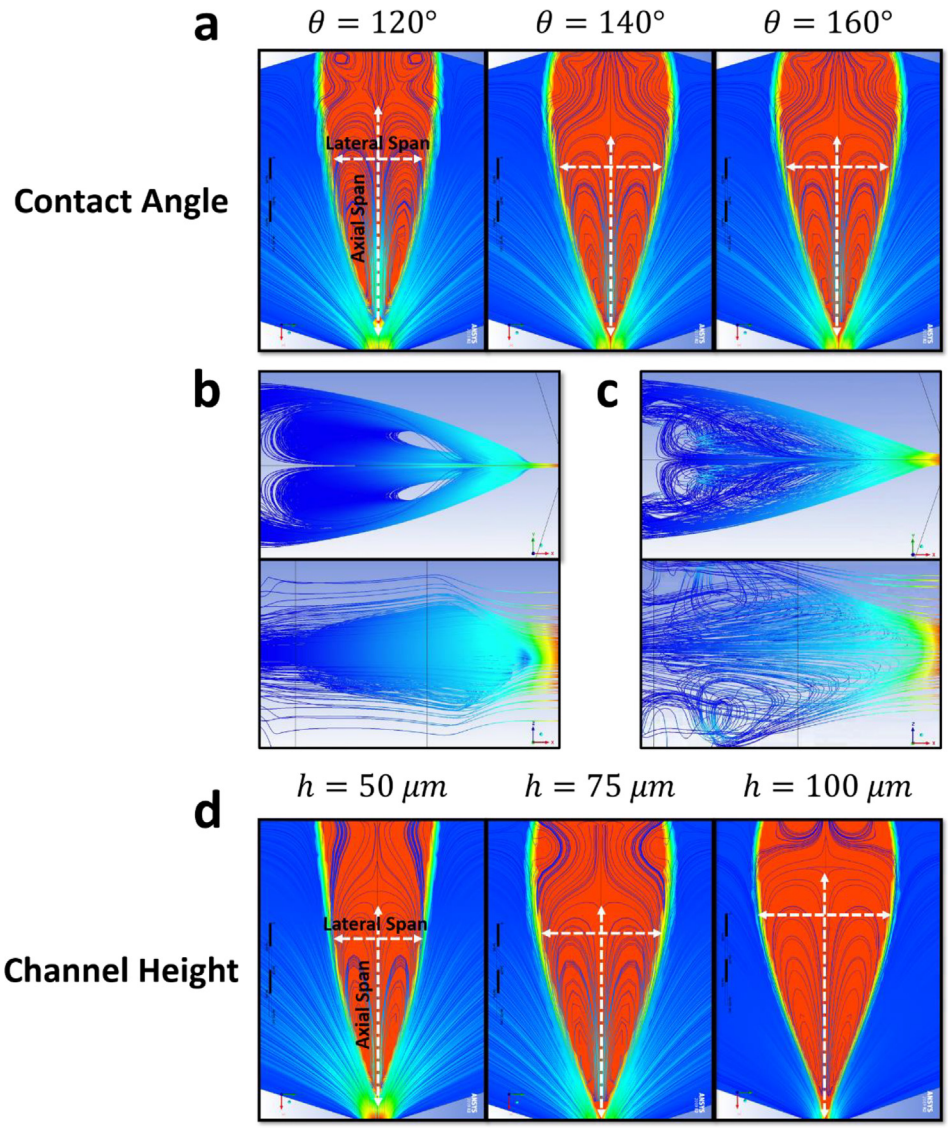

FIG. 7. (a) Comparison of microvortex geometry for different contact angles (PDMS surface treatments) (contact angle ↑: lateral span ↑ and axial span ↓) with the corresponding 3D streamlines for (b) $\theta = 120°$ and (c) $\theta = 160°$. (d) Comparison of microvortex geometry for different microchannel heights (channel height ↑: lateral span ↑ and axial span ↑). Multimedia views of the symmetric three-dimensional microvortices for low ($\theta = 120°$) and high ($\theta = 160°$) contact angle cases. Multimedia view: http://dx.doi.org/10.1063/5.0039179.5

channel height leads to a higher trapping efficiency especially since the microvortices become wider and can hold a higher number of cells without significant particle–particle interactions and trajectory shift due to the collisions.

VI. CONCLUSION

In this work, we performed an in-depth and comprehensive study of shear-dependent microvortices in liquid–liquid flow focusing geometries, which has shown promising results for high efficiency 1–1 droplet encapsulation. For this purpose, we utilized theoretical fluid mechanics, CFD modeling, and experimental fluid dynamics to study how these microvortices are formed and the factors affecting them. Our results indicate that the capillary number is one of the key parameters, which determines the generation of such microvortices. Specifically, these symmetric three-dimensional microvortices mostly occur at high *Ca* where the generation is in dripping and jetting regimes (not studied here). These microvortices enable trapping of particles/cells based on their sizes. In this study, we introduced d_{gap} as the trapping size threshold and, using theoretical fluid mechanics, correlated it with the orifice width and the flow rates of continuous and dispersed phases (power-law relation). The developed mathematical model matches well with the experimental results in predicting size-based particle trapping inside the microvortices. We also evaluated how PDMS hydrophobicity and channel heights affect the microvortex geometry. Our results indicate that increasing the hydrophobicity of the device results in an increase in the lateral span of the microvortices while reduces their axial span. In addition, increasing the channel height increases both the axial span and lateral span of the microvortices. Increasing both hydrophobicity and the channel height facilitates increasing the capacity of the system to trap a larger number of particles/cells and, consequently, improves trapping efficiency.

Building on this foundation, future work involves (i) exploring other key factors affecting the microvortices and (ii) improving the developed CFD model. In the present study, the compositions of the dispersed and continuous phases were fixed, as they result in stable droplet generation and interfacial shearing.[30] However, for widespread adoption of this technique, the effect of different compositions and, consequently, the viscosity ratio and interfacial tensions should be explored. The presence of particles in the flow can alter the flow streamlines[47] and increase the chance of particle–particle interaction. In this study, we maintained the particle concentration within limits to minimize these two effects. The future direction of this project will focus on the effect of particle concentration and size on the stability and effectiveness of microvortices. As for the CFD model, we used a coupled level set and VOF method to solve the multiphase flow problem. Such a model has been previously adopted for problems that require proper resolving of interfacial dynamics, particularly when thin films are present.[39,48,49] However, this model demands high computational costs because it requires extensive mesh refinement near wall interfaces and moving interfaces. For this, we will explore coupling the adaptive-mesh-refinement (AMR) method with our developed model.[50] Although our developed model accurately predicts the formation and dynamics of microvortices, it cannot accurately predict the size of droplets generated. This is because of droplet–droplet merging in our coupled level set and VOF model, which will be further explored in future works.

AUTHORS' CONTRIBUTIONS

G.K. and M.A. contributed equally to this work.

ACKNOWLEDGMENTS

The authors would like to acknowledge support from the National Science Foundation and the industrial members of the Center for Advanced Design and Manufacturing of Integrated Microfluidics (NSF I/UCRC Award No. IIP 1841509).

DATA AVAILABILITY

The data that support the findings of this study are available within the article.

REFERENCES

[1]H. N. Joensson and H. Andersson Svahn, "Droplet microfluidics—A tool for single-cell analysis", Angew. Chem. Int. Ed. **51**(49), 12176 (2012).
[2]E. Z. Macosko, A. Basu, R. Satija, J. Nemesh, K. Shekhar, M. Goldman, I. Tirosh, A. R. Bialas, N. Kamitaki, E. M. Martersteck, J. J. Trombetta, D. A. Weitz, J. R. Sanes, A. K. Shalek, A. Regev, and S. A. McCarroll, "Highly parallel genome-wide expression profiling of individual cells using nanoliter droplets", Cell **161**(5), 1202 (2015).
[3]A. M. Klein, L. Mazutis, I. Akartuna, N. Tallapragada, A. Veres, V. Li, L. Peshkin, D. A. Weitz, and M. W. Kirschner, "Droplet barcoding for single-cell transcriptomics applied to embryonic stem cells," Cell **161**(5), 1187 (2015).
[4]E. Brouzes, M. Medkova, N. Savenelli, D. Marran, M. Twardowski, J. Brian Hutchison, J. M. Rothberg, D. R. Link, N. Perrimon, and M. L. Samuels, "Droplet microfluidic technology for single-cell high-throughput screening," Proc. Natl. Acad. Sci. U. S. A. **106**(34), 14195 (2009).
[5]J. J. Agresti, E. Antipov, A. R. Abate, K. Ahn, A. C. Rowat, J.-C. Baret, M. Marquez, A. M. Klibanov, A. D. Griffiths, and D. A. Weitz, "Ultrahigh-throughput screening in drop-based microfluidics for directed evolution," Proc. Natl. Acad. Sci. U. S. A. **107**(9), 4004 (2010).
[6]S. Fiedler, S. G. Shirley, T. Schnelle, and G. Fuhr, "Dielectrophoretic sorting of particles and cells in a microsystem," Anal. Chem. **70**(9), 1909 (1998).
[7]T. Jiang, Y. Ren, W. Liu, D. Tang, Y. Tao, R. Xue, and H. Jiang, "Dielectrophoretic separation with a floating-electrode array embedded in microfabricated fluidic networks," Phys. Fluids **30**(11), 112003 (2018).
[8]N. Pamme and A. Manz, "On-chip free-flow magnetophoresis: continuous flow separation of magnetic particles and agglomerates," Anal. Chem. **76**(24), 7250 (2004).
[9]S.-C. S. Lin, X. Mao, and T. J. Huang, "Surface acoustic wave (SAW) acoustophoresis: now and beyond," Lab Chip **12**(16), 2766 (2012).
[10]P. Li, Z. Ma, Y. Zhou, D. J. Collins, Z. Wang, and Y. Ai, "Detachable acoustophoretic system for fluorescence-activated sorting at the single-droplet level," Anal. Chem. **91**(15), 9970 (2019).
[11]S. Duhr and D. Braun, "Why molecules move along a temperature gradient," Proc. Nat. Acad. Sci. **103**(52), 19678 (2006).
[12]S. M. Block, "Making light work with optical tweezers," Nature **360**(6403), 493 (1992).
[13]R. H. Cole, S.-Y. Tang, C. A. Siltanen, P. Shahi, J. Q. Zhang, S. Poust, Z. J. Gartner, and A. R. Abate, "Printed droplet microfluidics for on demand dispensing of picoliter droplets and cells," Proc. Natl. Acad. Sci. **114**(33), 8728 (2017).
[14]K. Samlali, F. Ahmadi, A. B. V. Quach, G. Soffer, and S. C. C. Shih, "Single cell isolation: One cell, one drop, one click: hybrid microfluidics for mammalian single cell isolation (Small 34/2020)," Small **16**(34), 2070190 (2020).
[15]M. A. Bijarchi, M. Dizani, M. Honarmand, and M. Behshad Shafii, "Splitting dynamics of ferrofluid droplets inside a microfluidic T-junction using a pulse-width modulated magnetic field in micro-magnetofluidics," Soft Matter **17**, 1317 (2021).
[16]D. Di Carlo, "Inertial microfluidics," Lab Chip **9**(21), 3038 (2009).
[17]H.-S. Moon, K. Je, J.-W. Min, D. Park, K.-Y. Han, S.-H. Shin, W.-Y. Park, C. E. Yoo, and S.-H. Kim, "Inertial-ordering-assisted droplet microfluidics for high-throughput single-cell RNA-sequencing," Lab Chip **18**(5), 775 (2018).
[18]T. V. Nizkaya, A. S. Gekova, J. Harting, E. S. Asmolov, and O. I. Vinogradova, "Inertial migration of oblate spheroids in a plane channel," Phys. Fluids **32**(11), 112017 (2020).
[19]A. M. Leshansky, A. Bransky, N. Korin, and U. Dinnar, "Tunable nonlinear viscoelastic "focusing" in a microfluidic device," Phys. Rev. Lett. **98**(23), 234501 (2007).
[20]M. Yamada, M. Nakashima, and M. Seki, "Pinched flow fractionation: Continuous size separation of particles utilizing a laminar flow profile in a pinched microchannel," Anal. Chem. **76**(18), 5465 (2004).
[21]G. K. Kurup and A. S. Basu, "Field-free particle focusing in microfluidic plugs," Biomicrofluidics **6**(2), 022008 (2012).
[22]H. Liu, M. Li, Y. Wang, J. Piper, and L. Jiang, "Improving single-cell encapsulation efficiency and reliability through neutral buoyancy of suspension," Micromachines **11**(1), 94 (2020).
[23]D. J. Collins, A. Neild, A. deMello, A.-Q. Liu, and Y. Ai, "The Poisson distribution and beyond: methods for microfluidic droplet production and single cell encapsulation," Lab Chip **15**(17), 3439 (2015).
[24]Y.-C. Tan, K. Hettiarachchi, M. Siu, Y.-R. Pan, and A. P. Lee, "Controlled microfluidic encapsulation of cells, proteins, and microbeads in lipid vesicles," J. Am. Chem. Soc. **128**(17), 5656 (2006).
[25]L. Li, P. Wu, Z. Luo, L. Wang, W. Ding, T. Wu, J. Chen, J. He, Y. He, H. Wang, Y. Chen, G. Li, Z. Li, and L. He, "Dean flow assisted single cell and bead encapsulation for high performance single cell expression profiling," ACS Sens. **4**(5), 1299 (2019).
[26]M. Chabert and J.-L. Viovy, "Microfluidic high-throughput encapsulation and hydrodynamic self-sorting of single cells," Proc. Natl. Acad. Sci. **105**(9), 3191 (2008).
[27]T. Jing, R. Ramji, M. E. Warkiani, J. Han, C. T. Lim, and C.-H. Chen, "Jetting microfluidics with size-sorting capability for single-cell protease detection," Biosens. Bioelectron. **66**, 19 (2015).
[28]J. F. Edd, D. Di Carlo, K. J. Humphry, S. Köster, D. Irimia, D. A. Weitz, and M. Toner, "Controlled encapsulation of single-cells into monodisperse picolitre drops," Lab Chip **8**(8), 1262 (2008).
[29]E. W. M. Kemna, R. M. Schoeman, F. Wolbers, I. Vermes, D. A. Weitz, and A. van den Berg, "High-yield cell ordering and deterministic cell-in-droplet encapsulation using Dean flow in a curved microchannel," Lab Chip **12**(16), 2881 (2012).

[30]G. Kamalakshakurup and A. P. Lee, "High-efficiency single cell encapsulation and size selective capture of cells in picoliter droplets based on hydrodynamic micro-vortices," Lab Chip **17**(24), 4324 (2017).
[31]Y.-C. Tan, V. Cristini, and A. P. Lee, "Monodispersed microfluidic droplet generation by shear focusing microfluidic device," Sens. Actuators B **114**(1), 350 (2006).
[32]G. F. Christopher and S. L. Anna, "Microfluidic methods for generating continuous droplet streams," J. Phys. D **40**(19), R319 (2007).
[33]C. Wang, S. V. Jalikop, and S. Hilgenfeldt, "Size-sensitive sorting of microparticles through control of flow geometry," Appl. Phys. Lett. **99**(3), 034101 (2011).
[34]M. V. Patel, I. A. Nanayakkara, M. G. Simon, and A. P. Lee, "Cavity-induced microstreaming for simultaneous on-chip pumping and size-based separation of cells and particles," Lab Chip **14**(19), 3860 (2014).
[35]S. Tomotika and G. I. Taylor, "On the instability of a cylindrical thread of a viscous liquid surrounded by another viscous fluid," Proc. R Soc. London, Ser. A **150**(870), 322 (1935).
[36]T. Ward, M. Faivre, M. Abkarian, and H. A. Stone, "Microfluidic flow focusing: Drop size and scaling in pressure versus flow-rate-driven pumping," Electrophoresis **26**(19), 3716 (2005).
[37]Y.-Y. Tsui, C.-Y. Liu, and S.-W. Lin, "Coupled level-set and volume-of-fluid method for two-phase flow calculations," Numer. Heat Transfer, Part B **71**(2), 173 (2017).
[38]M. Dianat, M. Skarysz, and A. Garmory, "A coupled level set and volume of fluid method for automotive exterior water management applications," Int. J. Multiphase Flow **91**, 19 (2017).
[39]M. Aghaamoo, Z. Zhang, X. Chen, and J. Xu, "Deformability-based circulating tumor cell separation with conical-shaped microfilters: Concept, optimization, and design criteria," Biomicrofluidics **9**(3), 034106 (2015).
[40]M. Bauer, M. Ataei, M. Caicedo, K. Jackson, M. Madou, and L. Bousse, "Burst valves for commercial microfluidics: A critical analysis," Microfluid. Nanofluid. **23**(7), 86 (2019).
[41]R. Lin, J. S. Fisher, M. G. Simon, and A. P. Lee, "Novel on-demand droplet generation for selective fluid sample extraction," Biomicrofluidics **6**(2), 024103 (2012).
[42]P. Garstecki, M. J. Fuerstman, H. A. Stone, and G. M. Whitesides, "Formation of droplets and bubbles in a microfluidic T-junction—scaling and mechanism of break-up," Lab Chip **6**(3), 437 (2006).
[43]A. Hochstetter, R. Vernekar, R. H. Austin, H. Becker, J. P. Beech, D. A. Fedosov, G. Gompper, S.-C. Kim, J. T. Smith, G. Stolovitzky, J. O. Tegenfeldt, B. H. Wunsch, K. K. Zeming, T. Krüger, and D. W. Inglis, "Deterministic lateral displacement: Challenges and perspectives," ACS Nano **14**(9), 10784 (2020).
[44]N. Garg, T. M. Westerhof, V. Liu, R. Liu, E. L. Nelson, and A. P. Lee, "Whole-blood sorting, enrichment and in situ immunolabeling of cellular subsets using acoustic microstreaming," Microsyst. Nanoeng. **4**(1), 17085 (2018).
[45]E. Sollier, D. E. Go, J. Che, D. R. Gossett, S. O'Byrne, W. M. Weaver, N. Kummer, M. Rettig, J. Goldman, N. Nickols, S. McCloskey, R. P. Kulkarni, and D. Di Carlo, "Size-selective collection of circulating tumor cells using Vortex technology," Lab Chip **14**(1), 63 (2014).
[46]B. M. Haines and A. L. Mazzucato, "A proof of Einstein's effective viscosity for a dilute suspension of spheres," SIAM J. Math. Anal. **44**(3), 2120 (2012).
[47]Q.-V. Do, D.-A. Van, V.-B. Nguyen, and V.-S. Pham, "A numerical modeling study on inertial focusing of microparticle in spiral microchannel," AIP Adv. **10**(7), 075017 (2020).
[48]Z. Zhang, J. Xu, B. Hong, and X. Chen, "The effects of 3D channel geometry on CTC passing pressure – towards deformability-based cancer cell separation," Lab Chip **14**(14), 2576 (2014).
[49]M. Besanjideh, A. Shamloo, and S. Kazemzadeh Hannani, "Enhanced oil-in-water droplet generation in a T-junction microchannel using water-based nanofluids with shear-thinning behavior: A numerical study," Phys. Fluids **33**(1), 012007 (2021).
[50]M. A. Hashem, A. Aghilinejad, X. Chen, and H. Tan, "Compound droplet modeling for circulating tumor cell microfiltration with adaptive meshing refinement," J. Fluids Eng. **142**(11), 111403 (2020).